CHALMERS | UNIVERSITY OF GOTHENBURG

PREPRINT 2014:25

Numerical studies of an adaptive finite element method applied to the reconstruction of shapes of buried objects from experimental data

LARISA BEILINA
NGUYEN TRUNG THÀNH
MICHAEL V. KLIBANOV
JOHN BONDESTAM MALMBERG

Department of Mathematical Sciences
Division of Mathematics
CHALMERS UNIVERSITY OF TECHNOLOGY
UNIVERSITY OF GOTHENBURG
Gothenburg Sweden 2014

Preprint 2014:25

Numerical studies of an adaptive finite element method applied to the reconstruction of shapes of buried objects from experimental data

Larisa Beilina, Nguyen Trung Thành, Michael V. Klibanov, John Bondestam Malmberg

Department of Mathematical Sciences
Division of Mathematics
Chalmers University of Technology and University of Gothenburg
SE-412 96 Gothenburg, Sweden
Gothenburg, December 2014

Preprint 2014:25
ISSN 1652-9715

Matematiska vetenskaper
Göteborg 2014

Numerical studies of an adaptive finite element method applied to the reconstruction of shapes of buried objects from experimental data

Larisa Beilina[1], Nguyen Trung Thành[2], Michael V. Klibanov[3] and John Bondestam Malmberg[4]

Abstract We perform extended studies of an adaptive finite element method applied to the reconstruction of shapes of buried objects from experimental backscattering data. We use experimental data which are collected by a microwave scattering facility located at the University of North Carolina at Charlotte, USA. Our numerical tests show accurate imaging of three components of interest of targets: shapes, locations and refractive indices.

1 Introduction

In this paper we present extended studies of an adaptive finite element method which we use to improve reconstruction of shapes of buried objects in the dry sand from experimental time-dependent backscattering data. First part of this study was presented in [10]. Experimental data were collected using a microwave scattering facility located at the University of North Carolina at Charlotte, USA. For the description of data collection procedure we refer to recent works [8, 19].

We consider a coefficient inverse problem (CIP) for Maxwell's equations in three dimensions. This paper is a continuation of our recent studies on this topic [8, 9, 19], where we have reconstructed shapes, locations and refractive indices of targets placed in air. To solve our CIP we use the two-stage numerical procedure presented in [5–7, 9]: on the first stage the approximately globally convergent method

[1]Corresponding author. Department of Mathematical Sciences, Chalmers University of Technology and Gothenburg University, SE-42196 Gothenburg, Sweden, (larisa@chalmers.se)

[2]Department of Mathematics, Iowa State University, Ames, IA, USA, (thanh@iastate.edu)

[3]Department of Mathematics and Statistics University of North Carolina at Charlotte, Charlotte, NC 28223, USA, (mklibanv@uncc.edu)

[4]Department of Mathematical Sciences, Chalmers University of Technology and Gothenburg University, SE-42196 Gothenburg, Sweden, (john.bondestam.malmberg@chalmers.se)

of [5] is applied to get a good first approximation for the exact solution of our CIP, and on the second stage the local adaptive finite element method of [2] refines the solution obtained on the first stage using the minimization of a Tikhonov functional. It make sense to refine the solution obtained on the first stage since in [15] was shown that a minimizer of the Tikhonov functional is closer to the exact solution than the first guess for this solution. In [7] the relaxation property was shown for mesh refinements. It states that the solution obtained on the refined mesh will be closer to the minimizer of a Tikhonov functional than the solution obtained on the coarse mesh. Using results of [7, 15] we conclude that we can obtain better approximations and shapes of objects through the minimization of a Tikhonov functional on the adaptively refined meshes.

An outline of this paper is as follows. In sections 2, 3 we state the forward and inverse problems on the first and the second stage, respectively. In Section 4 we describe the mesh refinement recommendation and the adaptive algorithm. In Section 5 we present numerical studies of the adaptive finite element method.

2 Statement of Forward and Inverse Problems on the first stage

In this section we state the forward and inverse problems which we use on the first stage.

Let $\Omega \subset \mathbb{R}^3$ be a convex bounded domain with the boundary $\partial\Omega \in C^3$, $\mathbf{x} = (x, y, z) \in \mathbb{R}^3$ and $C^{k+\alpha}$ denote a Hölder space where $k \geq 0$ is an integer and $\alpha \in (0, 1)$. On the first stage we model the wave propagation by the following Cauchy problem for the scalar wave equation

$$\varepsilon_{\mathrm{r}}(\mathbf{x}) \frac{\partial^2 u}{\partial t^2}(\mathbf{x}, t) - \Delta u(\mathbf{x}, t) = \delta(z - z_0) f(t), \qquad (\mathbf{x}, t) \in \mathbb{R}^3 \times (0, \infty), \tag{1}$$

$$u(\mathbf{x}, 0) = 0, \quad \frac{\partial u}{\partial t}(\mathbf{x}, 0) = 0, \qquad \mathbf{x} \in \mathbb{R}^3. \tag{2}$$

Here $f(t) \not\equiv 0$ is the waveform incident plane wave generated at the plane $\{z = z_0\}$ and propagating along the z-axis. We consider the propagation of the electric wave $E(\mathbf{x}, t) = (E_1, E_2, E_3)(\mathbf{x}, t)$ in $\mathbb{R}^3$ generated by the incident plane wave. In our experiments only the single non-zero component E_2 of the incident electric field $E(\mathbf{x}, t)$ is excited while two other components are set to zero, and we measure the backscattering function E_2, which is the voltage. On the first stage we use only the single equation (1) with $u = E_2$ instead of the full Maxwell's system. We do such approximation since it was shown numerically in [3] that the component E_2 of the electric field E dominates two other components. This observation is also confirmed by our experimental numerical studies - see Figure 1.

The function $\varepsilon_{\mathrm{r}}(\mathbf{x}) = \frac{\varepsilon(\mathbf{x})}{\varepsilon_0}$ in (1) is the relative dielectric constant, where $\varepsilon(\mathbf{x})$ is the absolute dielectric permittivity of the material and ε_0 is the dielectric permittivity of vacuum. We assume that ε_{r} is unknown inside the domain $\Omega \subset \mathbb{R}^3$ and this function is known outside of it,

$$\varepsilon_{\mathrm{r}} \in C^{\alpha}\left(\mathbb{R}^{3}\right), \quad \varepsilon_{\mathrm{r}}(\mathbf{x}) \in [1,b] \text{ for } \mathbf{x} \in \mathbb{R}^{3}, \quad \varepsilon_{\mathrm{r}}(\mathbf{x}) = 1 \text{ for } \mathbf{x} \in \mathbb{R}^{3} \setminus \Omega, \tag{3}$$

where $b > 1$ is a known constant. In our experiments the plane wave $f(t)$ is initialized outside of the domain $\overline{\Omega}$, that is, $\{z = z_0\} \cap \overline{\Omega} = \varnothing$.

Coefficient Inverse Problem 1 (CIP1). *Determine the function $\varepsilon_{\mathrm{r}}(\mathbf{x})$ for $\mathbf{x} \in \Omega$ with a known function g for a single incident plane wave generated at the plane $\{z = z_0\}$ outside of $\overline{\Omega}$:*

$$u(\mathbf{x},t) = g(\mathbf{x},t)\ \forall (\mathbf{x},t) \in \Gamma \times (0,\infty).$$

Here, $\Gamma \subset \partial\Omega$ is a backscattering part of the boundary $\partial\Omega$.

Remark 1.

- The data function g is extended numerically to a function $\tilde{g}$ on the whole boundary $\partial\Omega$, see Section 4 of [9]. Thus, we assume that $g(\mathbf{x},t)$ is known for every $(\mathbf{x},t) \in \partial\Omega \times (0,T)$.
- Global uniqueness theorems for multidimensional CIPs with a single measurement are currently known only under the assumption that at least one of initial conditions does not equal zero in the entire domain $\overline{\Omega}$ [5, 12]. In the case of our CIP we simply assume that uniqueness of our CIP holds.
- To solve CIP1 of the first stage we use the globally convergent method of [5]. Extended numerical studies of this method for the case of experimental backscattering data are presented in [8, 9, 18, 19].

3 Statement of Forward and Inverse Problems on the second stage

On the second stage we model the electric wave propagation in an isotropic and non-magnetic space in $\mathbb{R}^3$ with the dimensionless relative magnetic permeability $\mu_{\mathrm{r}} = 1$ and with the relative dielectric constant $\varepsilon_{\mathrm{r}}(\mathbf{x})$. We consider the following Cauchy problem as the model problem for the electric field $E(\mathbf{x},t) = (E_1, E_2, E_3)(\mathbf{x},t)$

$$\begin{aligned}
&\varepsilon_{\mathrm{r}}(\mathbf{x})\frac{\partial^2 E}{\partial t^2}(\mathbf{x},t) + \nabla \times \left(\nabla \times E(\mathbf{x},t)\right) = F(z,t), && (\mathbf{x},t) \in \mathbb{R}^3 \times (0,T),\\
&\nabla \cdot \left(\varepsilon_{\mathrm{r}}(\mathbf{x}) E(\mathbf{x},t)\right) = 0, && (\mathbf{x},t) \in \mathbb{R}^3 \times (0,T),\\
&E(\mathbf{x},0) = 0, \quad \frac{\partial E}{\partial t}(\mathbf{x},0) = 0, && \mathbf{x} \in \mathbb{R}^3.
\end{aligned} \tag{4}$$

Here $F(z,t) = (0, \delta(z - z_0) f(t), 0)$, $f(t) \not\equiv 0$, is the incident plane wave. We assume that the coefficient ε_{r} of equation (4) is the same as in (3). Let again $\Gamma \subset \partial\Omega$ be a backscattering part of the boundary $\partial\Omega$.

Coefficient Inverse Problem 2 (CIP2). *Determine the function* $\varepsilon_{\mathrm{r}}(\mathbf{x})$, $\mathbf{x} \in \Omega$, *assuming that the following vector function* $\mathbf{g}(\mathbf{x},t) = (g_1, g_2, g_3)(\mathbf{x},t)$ *is known for a single incident plane wave:*

$$E(\mathbf{x},t) = \mathbf{g}(\mathbf{x},t), \ \forall (\mathbf{x},t) \in \Gamma \times (0,T). \tag{5}$$

In (5) the vector function $\mathbf{g}$ models time dependent measurements of the electric field at the part Γ of the boundary $\partial\Omega$ of the domain Ω. As in the case of CIP1 we again assume that we have uniqueness for our CIP2.

The function E_2 in (4) models the voltage of one component of the electric field $E(\mathbf{x},t)$ which we measure in experiments. In our computer simulations of Section 5.4, E_2 is the only non-zero component of the incident filed. The other two components, E_1 and E_3, of electrical field are generated by the computed solution of problem (4) with the known value of $\varepsilon_{\mathrm{r}}(\mathbf{x}) \in \Omega$ which we have obtained as the solution of CIP1 via the approximate globally convergent algorithm on the first stage. Then the experimental data $\mathbf{g}$ are immersed into the computed component E_2 on the surface Γ.

3.1 The model problem

In our simulations we choose computational domain G such that $\Omega \subset G$ and $G = \Omega_{\mathrm{FEM}} \cup \Omega_{\mathrm{FDM}}$ with $\Omega_{\mathrm{FEM}} = \Omega$. We use domain decomposition finite element/finite difference method of [3] for the solution of the problem (4), where a finite element method is used in Ω_{FEM} and a finite difference method is used in Ω_{FDM}.

By (3) we have that

$$\begin{aligned} \varepsilon_{\mathrm{r}}(\mathbf{x}) &\geq 1, \text{ for } \mathbf{x} \in \Omega_{\mathrm{FEM}}, \\ \varepsilon_{\mathrm{r}}(\mathbf{x}) &= 1, \text{ for } \mathbf{x} \in \Omega_{\mathrm{FDM}}. \end{aligned}$$

We choose the domains Ω and G such that

$$\Omega = \Omega_{\mathrm{FEM}} = \left\{ \mathbf{x} = (x,y,z) : -a < x < a, -b < y < b, -c < z < c' \right\},$$

$$G = \{ \mathbf{x} = (x,y,z) : -A < x < A, -B < y < B, -C < z < z_0 \},$$

where $0 < a < A$, $0 < b < B$, $-C < -c < c' < z_0$, and $\Omega_{\mathrm{FDM}} = G \setminus \Omega_{\mathrm{FEM}}$. Denote by

$$\partial_1 G := \overline{G} \cap \{z = z_0\}, \quad \partial_2 G := \overline{G} \cap \{z = -C\}, \quad \partial_3 G := \partial G \setminus (\partial_1 G \cup \partial_2 G).$$

The backscattering side of Ω is $\Gamma = \partial\Omega \cap \{z = c'\}$. Next, define $\partial_i G_T := \partial_i G \times (0,T)$, $i = 1,2,3$. Let $t' \in (0,T)$ be a point in time after which the initialization of the plane wave at $\partial_1 G$ stops. We assume that the function $f(t) \in C[0,t']$.

Similarly with [3] we used stabilized model problem with the parameter $\xi \geq 1$:

$$
\begin{aligned}
&\varepsilon_{\mathrm{r}}(\mathbf{x}) \frac{\partial^2 E}{\partial t^2}(\mathbf{x},t) + \nabla\big(\nabla \cdot E(\mathbf{x},t)\big) - \nabla \cdot \big(\nabla E(\mathbf{x},t)\big) \\
&\qquad\qquad - \xi \nabla\Big(\nabla \cdot \big(\varepsilon_{\mathrm{r}}(\mathbf{x}) E(\mathbf{x},t)\big)\Big) = 0, \qquad (\mathbf{x},t) \in G \times (0,T), && (6)\\
&E(\mathbf{x},0) = 0, \quad \frac{\partial E}{\partial t}(\mathbf{x},0) = 0, \qquad \mathbf{x} \in G, && (7)\\
&E(\mathbf{x},t) = (0, f(t), 0), \qquad (\mathbf{x},t) \in \partial_1 G \times \big(0, t'\big], && (8)\\
&\frac{\partial E}{\partial n}(\mathbf{x},t) = -\frac{\partial E}{\partial t}(\mathbf{x},t), \qquad (\mathbf{x},t) \in \partial_1 G \times \big(t', T\big), && (9)\\
&\frac{\partial E}{\partial n}(\mathbf{x},t) = -\frac{\partial E}{\partial t}(\mathbf{x},t), \qquad (\mathbf{x},t) \in \partial_2 G_T, && (10)\\
&\frac{\partial E}{\partial n}(\mathbf{x},t) = 0, \qquad (\mathbf{x},t) \in \partial_3 G_T, && (11)
\end{aligned}
$$

where $\partial/\partial n$ is the normal derivative. Conditions (9) and (10) are first order absorbing boundary conditions [14]. At the lateral boundaries we impose a homogeneous Neumann condition (11). In [3] it was shown that the solution to the original Maxwell's equations is well approximated by the solution to (6)–(11) in the case where $\xi = 1$ and the discontinuities in ε_{r} are not too large. Here we have used the well-known identity $\nabla \times (\nabla \times E) = \nabla(\nabla \cdot E) - \nabla \cdot (\nabla E)$. We refer to [3] for details of the numerical solution of the forward problem (6)–(11).

3.2 The Tikhonov functional

Let Γ' be the extension of the backscattering side Γ up to the boundary $\partial_3 G$ of the domain G such that

$$\Gamma' = \left\{\mathbf{x} = (x,y,z) : -X < x < X,\ -Y < y < Y, z = c'\right\}.$$

Let G' be the part of the rectangular prism G which lies between the two planes Γ' and $\{z = -C\}$:

$$G' = \left\{\mathbf{x} = (x,y,z) : -X < x < X,\ -Y < y < Y,\ -C < z < c'\right\}.$$

Denote by $Q_T = G' \times (0,T)$, and $S_T = \partial G' \times (0,T)$.

In our CIP2 we have the data $\mathbf{g}$ in (5) only on Γ. These data are complemented on the rest of the boundary $\partial G'$ of the domain G' by simulated data using the immersing procedure of [9]. Thus, we can approximately get the vector function $\widetilde{\mathbf{g}}$:

$$\widetilde{\mathbf{g}}(\mathbf{x},t) = E(\mathbf{x},t), \quad (\mathbf{x},t) \in S_T. \tag{12}$$

To solve our inverse problem we minimize the Tikhonov functional:

$$F(E,\varepsilon_{\mathrm{r}}):=\frac{1}{2}\int_{S_T}\left(E(\mathbf{x},t)-\widetilde{\mathbf{g}}(\mathbf{x},t)\right)^2 z_\delta(t)\,\mathrm{d}\sigma\,\mathrm{d}t+\frac{1}{2}\gamma\int_G\left(\varepsilon_{\mathrm{r}}(\mathbf{x})-\varepsilon_{\mathrm{r,\,glob}}(\mathbf{x})\right)^2\mathrm{d}\mathbf{x}, \tag{13}$$

where $\gamma > 0$ is the (small) regularization parameter and $\varepsilon_{\mathrm{r,\,glob}}$ is the computed coefficient which we have obtained on the first stage via the globally convergent method. In our computations we use single value of the regularization parameter γ which we choose in a computational efficient way such that the values of $\gamma > 0$ give the smallest reconstruction error. We refer to [1, 13] for different techniques for the choice of regularization parameter. In (13) the function $z_\delta(t)$ is used to introduce the compatibility conditions at $\overline{Q}_T \cap \{t = T\}$ for the adjoint problem. The function $z_\delta(t)$ satisfies

$$z_\delta \in C^2\,[0,T]\,,\qquad \begin{cases} z_\delta(t)=1, & t\in(0,T-\delta)\,,\\ 0<z_\delta(t)<1, & t\in(T-\delta,T-\delta/2)\,,\\ z_\delta(t)=0, & t\in(T-\delta/2,T)\,. \end{cases}$$

Let E_{glob} be the solution of the forward problem (6)–(11) with $\varepsilon_{\mathrm{r}} := \varepsilon_{\mathrm{r,\,glob}}$. Denote by $p = \partial_n E_{\mathrm{glob}}|_{S_T}$. In addition to the Dirichlet condition (12), we set the Neumann boundary condition as

$$\frac{\partial E}{\partial n}(\mathbf{x},t)=p\,(\mathbf{x},t)\,,\quad (\mathbf{x},t)\in S_T.$$

Introduce the following spaces of real valued vector functions

$$H_E^1(Q_T)=\left\{f\in[H^1(Q_T)]^3: f(\mathbf{x},0)=0\right\},$$

$$H_\lambda^1(Q_T)=\left\{f\in[H^1(Q_T)]^3: f(\mathbf{x},T)=0\right\},$$

$$U^1=H_E^1(G_T)\times H_\lambda^1(G_T)\times B(G)\,,$$

where $B(G)$ is the space of functions bounded on G with the norm $\|f\|_{B(G)} = \sup_G |f|$.

To minimize the functional (13) we introduce the Lagrangian

$$\begin{aligned} L(E,\lambda,\varepsilon_{\mathrm{r}}) &= F(E,\varepsilon_{\mathrm{r}})-\int_{Q_T}\varepsilon_{\mathrm{r}}(\mathbf{x})\frac{\partial\lambda}{\partial t}(\mathbf{x},t)\cdot\frac{\partial E}{\partial t}(\mathbf{x},t)\,\mathrm{d}\mathbf{x}\,\mathrm{d}t\\ &\quad-\int_{Q_T}\nabla\cdot E(\mathbf{x},t)\nabla\cdot\lambda(\mathbf{x},t)\,\mathrm{d}\mathbf{x}\,\mathrm{d}t+\int_{Q_T}\nabla E(\mathbf{x},t)\nabla\lambda(\mathbf{x},t)\,\mathrm{d}\mathbf{x}\,\mathrm{d}t\\ &\quad+\xi\int_{Q_T}\nabla\cdot\left(\varepsilon_{\mathrm{r}}(\mathbf{x})E(\mathbf{x},t)\right)\nabla\cdot\lambda(\mathbf{x},t)\,\mathrm{d}\mathbf{x}\,\mathrm{d}t-\int_{S_T}\lambda(\mathbf{x},t)\cdot p(\mathbf{x},t)\,\mathrm{d}\sigma\,\mathrm{d}t, \end{aligned} \tag{14}$$

where E and λ are weak solutions of problems (16)–(18) and (19)–(21), respectively, see details in [9].

To derive the Fréchet derivative of the Lagrangian (14), we assume that in (14) the elements of the vector function $(E,\lambda,\varepsilon_{\mathrm{r}})$ can be varied independently of each other. We search for a point $w \in U^1$ such that

$$L'(w)(\overline{w}) = 0, \quad \forall \overline{w} \in U^1. \tag{15}$$

To find the Fréchet derivative $L'(w)$, we consider $L(w+\overline{w}) - L(w)$, for every $\overline{w} \in U^1$ and single out the linear part of the obtained expression. Then the forward problem in the domain G' is given by

$$\begin{aligned} &\varepsilon_{\mathrm{r}}(\mathbf{x}) \frac{\partial^2 E}{\partial t^2}(\mathbf{x},t) + \nabla\big(\nabla \cdot E(\mathbf{x},t)\big) \\ &\qquad - \nabla \cdot \big(\nabla E(\mathbf{x},t)\big) - \xi \nabla \Big(\nabla \cdot \big(\varepsilon_{\mathrm{r}}(\mathbf{x}) E(\mathbf{x},t)\big)\Big) = 0, \quad (\mathbf{x},t) \in Q_T, \end{aligned} \tag{16}$$

$$E(\mathbf{x},0) = 0, \quad \frac{\partial E}{\partial t}(\mathbf{x},0) = 0, \qquad \mathbf{x} \in G', \tag{17}$$

$$\frac{\partial E}{\partial n}(\mathbf{x},t) = p(\mathbf{x},t), \qquad (\mathbf{x},t) \in S_T. \tag{18}$$

The adjoint problem is:

$$\begin{aligned} &\varepsilon_{\mathrm{r}}(\mathbf{x}) \frac{\partial^2 \lambda}{\partial t^2}(\mathbf{x},t) + \nabla\big(\nabla \cdot \lambda(\mathbf{x},t)\big) \\ &\qquad - \nabla \cdot \big(\nabla \lambda(\mathbf{x},t)\big) - \xi \varepsilon_{\mathrm{r}}(\mathbf{x}) \nabla\big(\nabla \cdot \lambda(\mathbf{x},t)\big) = 0, \quad (\mathbf{x},t) \in Q_T, \end{aligned} \tag{19}$$

$$\lambda(\mathbf{x},T) = 0, \quad \frac{\partial \lambda}{\partial t}(\mathbf{x},T) = 0, \qquad \mathbf{x} \in G', \tag{20}$$

$$\frac{\partial \lambda}{\partial t}(\mathbf{x},t) = z_\delta(t)\big(\widetilde{\mathbf{g}}(\mathbf{x},t) - E(\mathbf{x},t)\big)(\mathbf{x},t), \qquad (\mathbf{x},t) \in S_T. \tag{21}$$

4 Mesh refinement recommendation and the adaptive algorithm

For the finite element discretization of Q_T we used stabilized finite element method of [3]. To do that we define a partition $K_h = \{K\}$ of G' which consists of tetrahedra. Here h is a mesh function defined as $h|_K = h_K$ — the local diameter of the element K. Let $J_\tau = \{J\}$ be a partition of the time interval $(0,T)$ into subintervals $J = (t_{k-1}, t_k]$ of uniform length $\tau = t_k - t_{k-1}$. We also assume the minimal angle condition on the K_h [11].

In our computations we have used local adaptive mesh refinements algorithm which is based on ideas of [4], Theorem 5.1 and the criterion of Remark 5.1 of [2]. From this criterion follows that the finite element mesh should be locally refined in such subdomain of Ω where the maximum norm of the Fréchet derivative of the objective functional is large. The Fréchet derivative of the functional (13) is:

$$
\begin{aligned}
L_h^{\prime,m}(\mathbf{x}) = &-\int_0^T \frac{\partial \lambda_h^m}{\partial t}(\mathbf{x},t)\cdot\frac{\partial E_h^m}{\partial t}(\mathbf{x},t)\,\mathrm{d}t \\
&+\xi\int_0^T \nabla\cdot E_h^m(\mathbf{x},t)\nabla\cdot\lambda_h^m(\mathbf{x},t)\,\mathrm{d}t+\gamma({\varepsilon_h}^m(\mathbf{x})-\varepsilon_{\mathrm{r,\,glob}}(\mathbf{x})).
\end{aligned}
\tag{22}
$$

Here, m is the number of iteration in the optimization procedure, and $(E_h^m, \lambda_h^m, \varepsilon_h^m)$ are finite element approximations of the functions $(E, \lambda, \varepsilon_{\mathrm{r}})$, see details in [2, 3].

Adaptive algorithm

- Step 0. Choose an initial mesh K_h in Ω and an initial time partition J_0 of the time interval $(0, T)$. Start from the initial guess $\varepsilon_h^0 = \varepsilon_{\mathrm{r,\,glob}}$. Compute the approximations ε_h^m in the following steps:
- Step 1. Compute the approximate solutions E_h^m and λ_h^m of the state problem (16)–(18) and the adjoint problem (19)–(21) on K_h and J_k, using coefficient ε_h^m, and compute the Fréchet derivative $L_h^{\prime,m}$ via (22).
- Step 2. Update the coefficient on K_h using the conjugate gradient method:

$$\varepsilon_h^{m+1}(\mathbf{x}) := \varepsilon_h^m(\mathbf{x}) + \alpha d^m(\mathbf{x}),$$

  where $\alpha > 0$ is a step-size in the conjugate gradient method and can be computed by a line search procedure, see, e.g. [17], and

$$d^m(\mathbf{x}) = -L_h^{\prime,m}(\mathbf{x}) + \beta^m d^{m-1}(\mathbf{x}),$$

  with

$$\beta^m = \frac{||L_h^{\prime,m}||^2_{L_2(\Omega)}}{||L_h^{\prime,m-1}||^2_{L_2(\Omega)}},$$

  and $d^0(\mathbf{x}) = -L_h^{\prime,0}(\mathbf{x})$.
- Step 3. Stop updating the coefficient and set $\varepsilon_h := \varepsilon_h^{m+1}$, $M := m+1$, if either $||L_h^{\prime,m}||_{L_2(\Omega)} \le \theta$ or norms $||\varepsilon_h^m||_{L_2(\Omega)}$ are stabilized. Here θ is a tolerance number. Otherwise, set $m := m+1$ and go to step 1.
- Step 4. Compute $L_h^{\prime,M}$ via (22). Refine the mesh at all grid points $\mathbf{x}$ where

$$|L_h^{\prime,M}(\mathbf{x})| \ge \beta_1 \max_{\mathbf{x}\in\overline{\Omega}} |L_h^{\prime,M}(\mathbf{x})|.$$

  Here the tolerance number $\beta_1 \in (0, 1)$ is chosen by the user.
- Step 5. Construct a new mesh K_h in Ω and a new partition J_k of the time interval $(0, T)$. On J_k the new time step τ should be chosen in such a way that the Courant-Friedrichs-Lewy (CFL) condition is satisfied. Interpolate the initial approximation $\varepsilon_{\mathrm{r,\,glob}}$ from the previous mesh to the new mesh. Next, return to step 1 at $m = 1$ and perform all above steps on the new mesh. Stop mesh refinements

if norms defined in step 3 either increase or stabilize, compared with the previous mesh.

5 Numerical studies

In this section we present results of reconstruction of shapes of buried objects placed inside a sandbox using the adaptive finite element method of Section 4. We obtain initial guesses in the Tikhonov functional (13) using the globally convergent algorithm on the first stage, see [9] for details and these initial guesses.

For the experimental data collection scheme we refer to [8, 18, 19]. We note that in this work we consider the objects placed inside a sandbox. To model buried objects in dry sand we used the fact that the relative dielectric constant of dry sand is $\varepsilon_{\mathrm{r}}\left(\mathrm{sand}\right) = 4$. Thus, in our computational studies of [10, 18] and of this work we scale our results of reconstruction by the factor 4. Tables 1 and 2 present results after scaling.

In our verification of the first stage we have used different types of targets, see Table 1 of [18] for the full description of all data sets. We are working with metallic objects as with dielectrics which have large dielectric constants, see [16, 18] for details, and we call them *appearing dielectric constants*. We choose values for *appearing dielectric constants* such that

$$\varepsilon_{\mathrm{r}}\left(\text{metallic target}\right) \geq 10. \tag{23}$$

To compare our computational results with directly measured refractive indices $n = \sqrt{\varepsilon_{\mathrm{r}}}$ of dielectric targets and appearing dielectric constants of metallic targets (see (23)), we consider only the maximal values of the computed functions ε_{r} obtained on the first and second stages of our two-stage numerical procedure. Thus, we define

$$\varepsilon_{\mathrm{r}}^{\mathrm{comp}} = \max_{\mathbf{x}\in\overline{\Omega}} \varepsilon_{\mathrm{r}}\left(\mathbf{x}\right), \quad n^{\mathrm{comp}} = \sqrt{\varepsilon_{\mathrm{r}}^{\mathrm{comp}}}. \tag{24}$$

5.1 Data preprocessing

In this work we have used the same data preprocessing procedure as was used in [10, 19]. Below we present main steps of our data preprocessing procedure:

1. Data propagation.
2. Extraction of the target's signal from the total signal. The total signal is a mixture of the signal from the target and the signal from the sand. This extraction is applied to the propagated data.
3. Data calibration: to scale the measured data to the same scaling as in our simulations. This was done by using calibrating objects.

For data propagation we have propagated the measured data to a *propagated plane*. This plane was located at about 4 cm from the targets. A data calibration procedure was used to scale the measured data by a certain *calibration factor* obtained in our computational simulations. The choice of this factor depends on the data of a known *calibrating object*. The procedure of the extraction of the signal of the target from the total signal is complicated, and it is described in [18].

5.2 Computational domains

The spatial domains in our experiments are set in meters. We choose our computational domain G as

$$G = \{\mathbf{x} = (x, y, z) \in (-0.56, 0.56) \times (-0.56, 0.56) \times (-0.16, 0.1)\}. \tag{25}$$

The boundary of the domain G is $\partial G = \partial_1 G \cup \partial_2 G \cup \partial_3 G$. Here, $\partial_1 G$ and $\partial_2 G$ are front and back sides of the domain G at $\{z = 0.1\}$ and $\{z = -0.16\}$, respectively, and $\partial_3 G$ is the union of left, right, top and bottom sides of this domain.

For the solution of the state problem (16)–(18) and the adjoint problem (19)–(21) we have used the domain decomposition finite element/finite difference method of [3]. To do that the the domain G is split into two subdomains $\Omega_{\mathrm{FEM}} = \Omega$ and Ω_{FDM} so that $G = \Omega_{\mathrm{FEM}} \cup \Omega_{\mathrm{FDM}}$ and inner domain is defined as

$$\Omega_{\mathrm{FEM}} = \Omega = \{\mathbf{x} = (x, y, z) \in (-0.5, 0.5) \times (-0.5, 0.5) \times (-0.1, 0.04)\}. \tag{26}$$

The experimental data for both stages are given at the front side Γ of the domain Ω which is defined as

$$\Gamma = \{\mathbf{x} = (x, y, z) \in \partial\Omega : z = 0.04\}. \tag{27}$$

5.3 Description of experimental data sets

Tables 1 and 2 describe the details of used data sets together with the burial depths of the targets. After obtaining computational results, the refractive indices of all dielectric targets were measured, and these measured refractive indices were compared to those predicted by the computations.

We note that the burial depths of the objects of Tables 1 and 2 varied between 2 cm and 10 cm. Such depths are relevant for military applications where the burial depths of antipersonnel land mines typically do not exceed 10 cm. The measured data of the sandbox (without buried objects) was used for the calibration of all data for the objects of Tables 1 and 2.

5.4 Numerical examples of the second stage

From results of [18, 19] we can conclude that the first stage provides accurate locations and accurate values of the refractive indices $n = \sqrt{\varepsilon_{\mathrm{r}}}$ of the dielectric targets as well as large values of appearing dielectric constants ε_{r} for the metallic targets. However, the globally convergent algorithm does not reconstruct shapes well, see Figure 4 in [10]. To refine shapes, we have used the second stage, on which we have minimized the Tikhonov functional on locally adaptively refined meshes.

Our experimental backscattering data at the second stage are given only for the second component E_2 of the electric field E in (5) and are measured on the front side Γ of the domain Ω defined as in (27). For generation of other two components E_1 and E_3 we solve the forward problem (6)–(11) in the computational domain G defined as in the first stage in (25) with the known value of ε_{r} which we take from the first stage of our two-stage numerical procedure. Then we apply the data immersing procedure described in Section 7.3.3 of [9] to solve the inverse problem via the algorithm of Section 4. The immersing procedure of [9] first immerses the time-dependent propagated experimental data $g(\mathbf{x},t) = E_2(\mathbf{x},t)|_{\mathbf{x}\in\Gamma}$ into the computationally simulated data and then extends the data g from Γ to Γ'.

We choose the waveform f in (6)–(11) as

$$f(t) = \sin(\omega t), \quad 0 \le t \le t' := \frac{2\pi}{\omega},$$

where we use $\omega = 30$ and $T = 1.2$. We solve the problem (6)–(11) using the explicit scheme of [3] with the time step size $\tau = 0.003$, which satisfies the CFL condition.

We obtain the image of the dielectric targets based on the function $\varepsilon_{\mathrm{r,\,diel}}$, which we define as

$$\varepsilon_{\mathrm{r,\,diel}}(\mathbf{x}) = \begin{cases} \varepsilon_{\mathrm{r}}(\mathbf{x}) \text{ if } \varepsilon_{\mathrm{r}}(\mathbf{x}) \ge \beta_{\mathrm{diel}} \max_{\mathbf{x}\in\overline{\Omega}} \varepsilon_{\mathrm{r}}(\mathbf{x}), \\ 1 \text{ otherwise.} \end{cases}$$

For metallic targets we use a similar function $\varepsilon_{\mathrm{r,\,metal}}$,

$$\varepsilon_{\mathrm{r,\,metal}}(\mathbf{x}) = \begin{cases} \varepsilon_{\mathrm{r}}(\mathbf{x}) \text{ if } \varepsilon_{\mathrm{r}}(\mathbf{x}) \ge \beta_{\mathrm{metal}} \max_{\mathbf{x}\in\overline{\Omega}} \varepsilon_{\mathrm{r}}(\mathbf{x}), \\ 1 \text{ otherwise.} \end{cases}$$

Here, β_{deil}, $\beta_{\mathrm{metal}} \in (0,1)$ and ε_{r} is the function computed by the algorithm of Section 4. In general, β_{deil} and β_{metal} may be different, but in this study we have $\beta_{\mathrm{deil}} = \beta_{\mathrm{metal}} = 0.5$.

Tables 1 and 2 display computed and directly measured refractive indices of dielectric objects as well as appearing dielectric constants for metallic objects, respectively, their correct and calculated burial depths obtained on the first stage. On the second stage we have obtained refractive indices of dielectric targets and appearing dielectric constants of metallic targets very close to ones of the first stage, see Table 3.

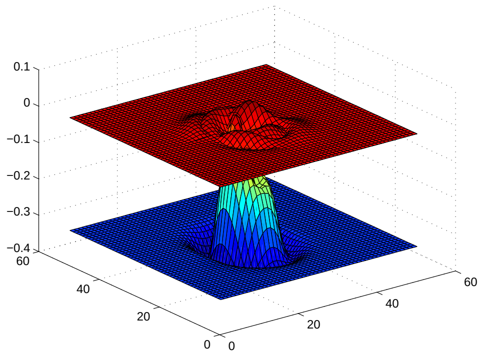

a)

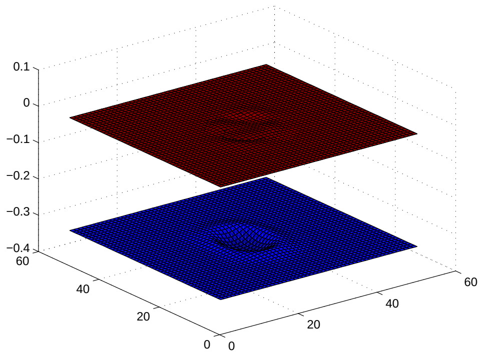

b)

Fig. 1 Backscattering simulated data of the electric field $E(\mathbf{x},t) = (E_1,E_2,E_3)(\mathbf{x},t)$ of the electric field at time $t = 0.3$: a) for Object #1 of Table 2; b) for Object #3 of Table 1. We observe that the component E_2 of the electric field E dominates by amplitude two other components E_1,E_3 which are located very close to each other and are not distinguishable on this figure.

Figure 1 shows simulated backscattering data for all three components of the electric field $E(\mathbf{x},t)$ for Object #1 of Table 2 and Object #3 of Table 1, respectively. To simulate these data we solve the problem (6)–(11) numerically with the known values of the function $\varepsilon_{\rm r} = \varepsilon_{\rm r,\,glob}$ obtained at the first stage. We observe that the component E_2 of the electric field E dominates by amplitude two other components E_1,E_3 for both objects. Figures 2, 3 show backscattering immersed data of the second component of electric field E_2 for Object #1 of Table 2 (metallic ball) and for Object #3 of Table 1 (ceramic mug), respectively, at different times.

Figures 4–7 show adaptively refined meshes and obtained reconstructions on these meshes for Objects #1, #2, #5, and #6, respectively. The results for adaptively refined meshes for all objects of Tables 1 and 2 are summarized in Table 3. Using Table 3 we observe that local refinement of the mesh does not have a significant increase in the number of nodes and elements in the coarse finite element grid. This fact indicates towards efficiency of the application of adaptive algorithm to the solution of our CIP. Using Figures 4–7 and results of Table 3 we can conclude that the locations as well as the shapes of most targets are significantly improved on the second stage of our two-stage numerical procedure.

Object #	Description	Computed depth (cm)	Exact depth (cm)	Depth error (%)	Computed n	Measured n	Refractive index error (%)
2	Bottle filled with clear water	3.6	4.0	10	4.7	4.88	4
3	Ceramic mug	4.0	5.0	20	1.0	1.39	21
6	Wet wooden block	5.5	9.8	44	4.2	4.016	1

Table 1 Results of the first stage: descriptions, burial depths, and refractive indices $n = \sqrt{\varepsilon_r}$ of non-metallic targets. Errors are computed relative to the exact/measured value. Numbers for objects are chosen to be consistent with those of [10].

Object #	Description	Computed depth (cm)	Exact depth (cm)	Depth error (%)	Computed ε_r
1	Metallic ball	2.9	3.0	3	31.0
4	Two metallic blocks, separated by 1 cm	3.8 4.0	4.0 4.0	5 0	99.8 56.5
5	Metallic prism	1.0	2.0	50	50.0
7	Two metallic prisms, separated by 6 cm	3.0 3.6	3.0 3.0	0 20	23.4 30.5
8	Two metallic prisms, separated by 6 cm	7.3 8.2	10.0 10.0	27 18	23.4 30.5

Table 2 Results of the first stage: descriptions, burial depths, and estimated effective dielectric constants of metallic targets. Object #4 consists of two metallic targets with 1 cm distance between their surfaces (a case of superresolution, see details in [10]). Object #7 and Object #8 consist of the same two metallic targets, but at different depths. Errors are computed relative to the exact value. Numbers for objects are chosen to be consistent with those of [10].

Object #		coarse mesh	1 ref. mesh	2 ref. mesh	3 ref. mesh	4 ref. mesh
1	# nodes	21853	21947	22211	22606	
	# elements	115200	115488	116868	119448	
	$\varepsilon_r^{\text{comp}}$	24.5	24.6	24.7	24.6	
2	# nodes	21853	21901	22231	22882	
	# elements	115200	115488	117056	120912	
	n^{comp}	4.7	4.7	4.7	4.7	
3	# nodes	21853	21893			
	# elements	115200	115440			
	n^{comp}	1.0	1.0			
4	# nodes	21853	21961	22448	23228	
	# elements	115200	115848	118034	122962	
	$\varepsilon_r^{\text{comp}}$	75.6	100.0	100.0	100.0	
5	# nodes	21853	21953	22438	23195	
	# elements	115200	115800	117996	122784	
	$\varepsilon_r^{\text{comp}}$	52.0	52.0	51.2	50.4	
6	# nodes	21853	21978	22432		
	# elements	115200	115950	117938		
	n^{comp}	4.3	4.3	4.4		
7	# nodes	21853	22003	22489	23214	24274
	# elements	115200	116100	118226	122840	129200
	$\varepsilon_r^{\text{comp}}$	32.8	33.2	34.9	36.7	38.4
8	# nodes	21853	21992	22463	23138	24040
	# elements	115200	116034	118094	122432	127816
	$\varepsilon_r^{\text{comp}}$	31.4	32.7	34.5	37.4	39.0

Table 3 Results of the second stage: Numbers of nodes and elements in adaptively refined meshes for the objects of Tables 1 and 2. For dielectric objects, computed refractive indices n^{comp} are shown, while for metallic objects appearing dielectric constants $\varepsilon_r^{\text{comp}}$ are shown. (See equation (24) for definitions of n^{comp} and $\varepsilon_r^{\text{comp}}$). If after a certain number of refinements no further data are presented for a particular object, the computations converged at the last presented step for that object.

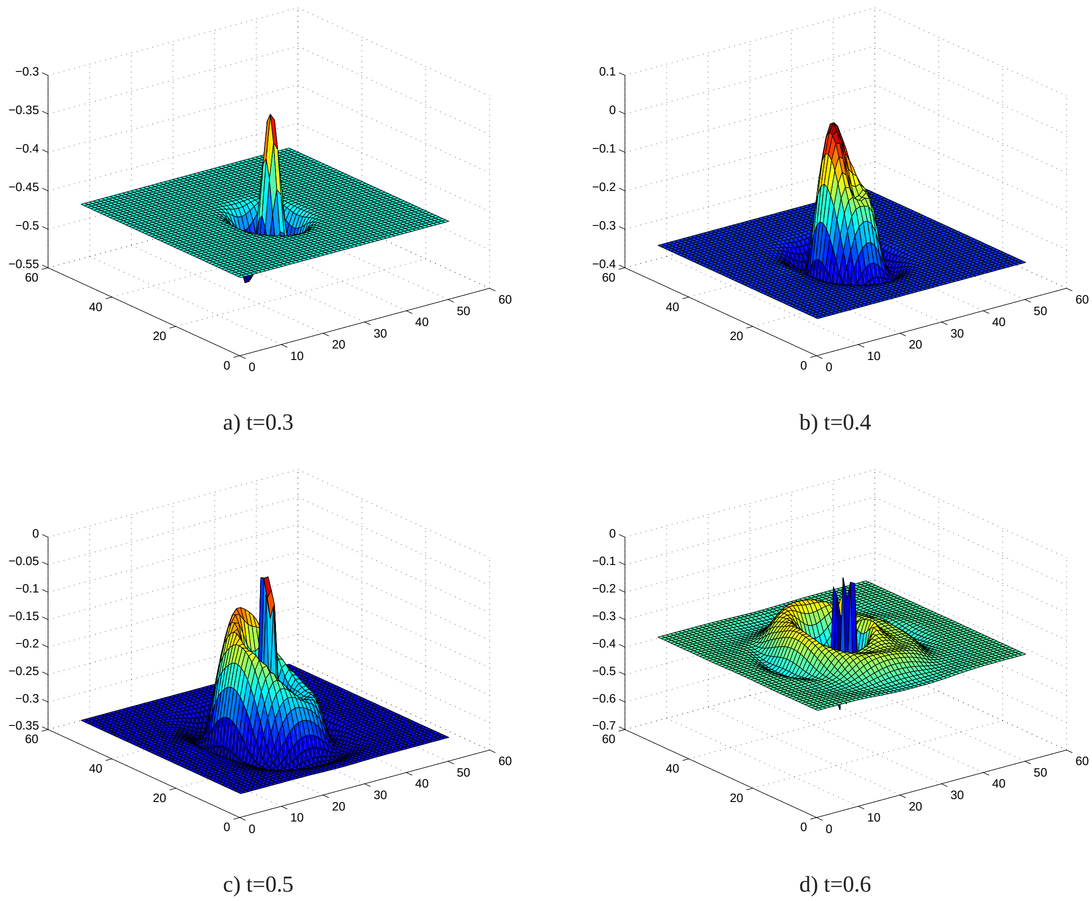

a) t=0.3 b) t=0.4

c) t=0.5 d) t=0.6

Fig. 2 Backscattering immersed data of the second component E_2 of the electric field for Object #1 of Table 2, without presence of signal from sand. Recall that the final time is $T = 1.2$.

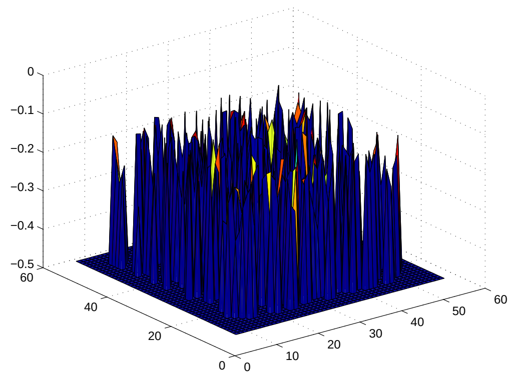

a) t=0.3

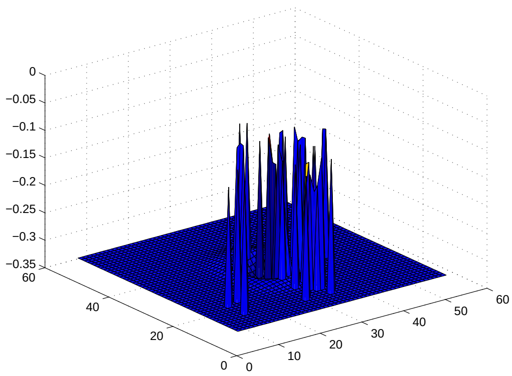

b) t=0.4

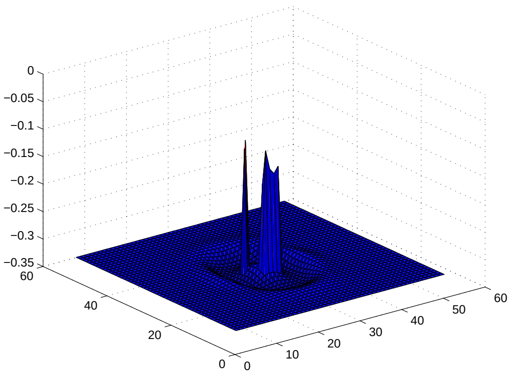

c) t=0.5

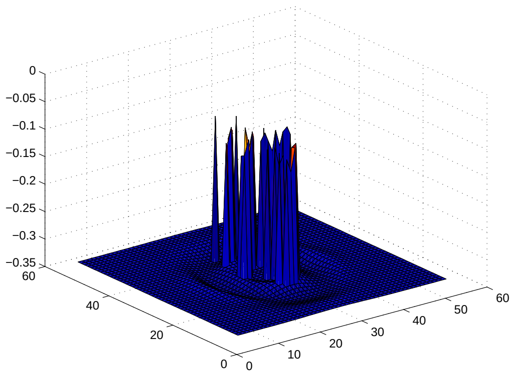

d) t=0.6

Fig. 3 Backscattering immersed data of the second component E_2 of the electric field for Object #3 of Table 1, without presence of signal from sand. Recall that the final time is $T = 1.2$.

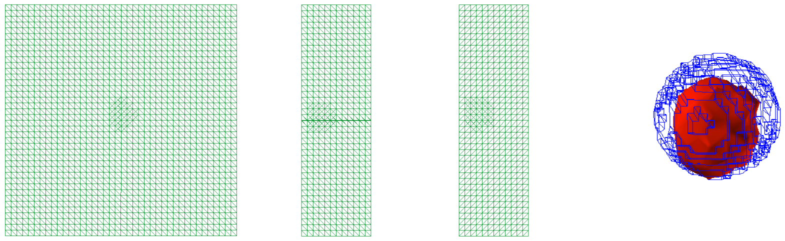

(a) 1 ref mesh, *xy*-view (b) *xz*-view (c) *yz*-view (d) $\varepsilon_r^{comp} \approx 24.6$

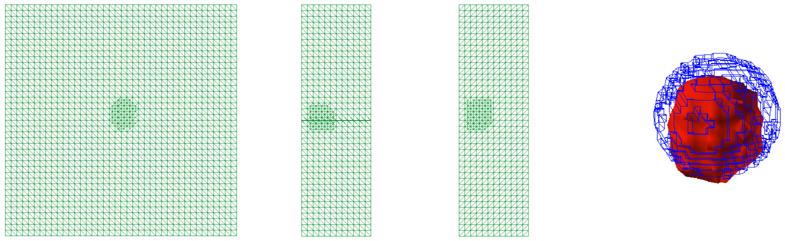

(e) 2 ref mesh, *xy*-view (f) *xz*-view (g) *yz*-view (h) $\varepsilon_r^{comp} \approx 24.7$

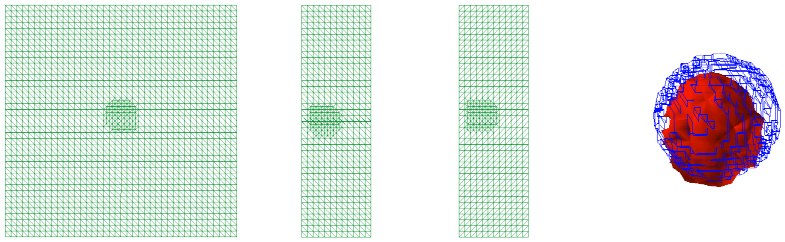

(i) 3 ref mesh, *xy*-view (j) *xz*-view (k) *yz*-view (l) $\varepsilon_r^{comp} \approx 24.6$

Fig. 4 Adaptively refined meshes for Object #1 of Table 2 and respective reconstructions.

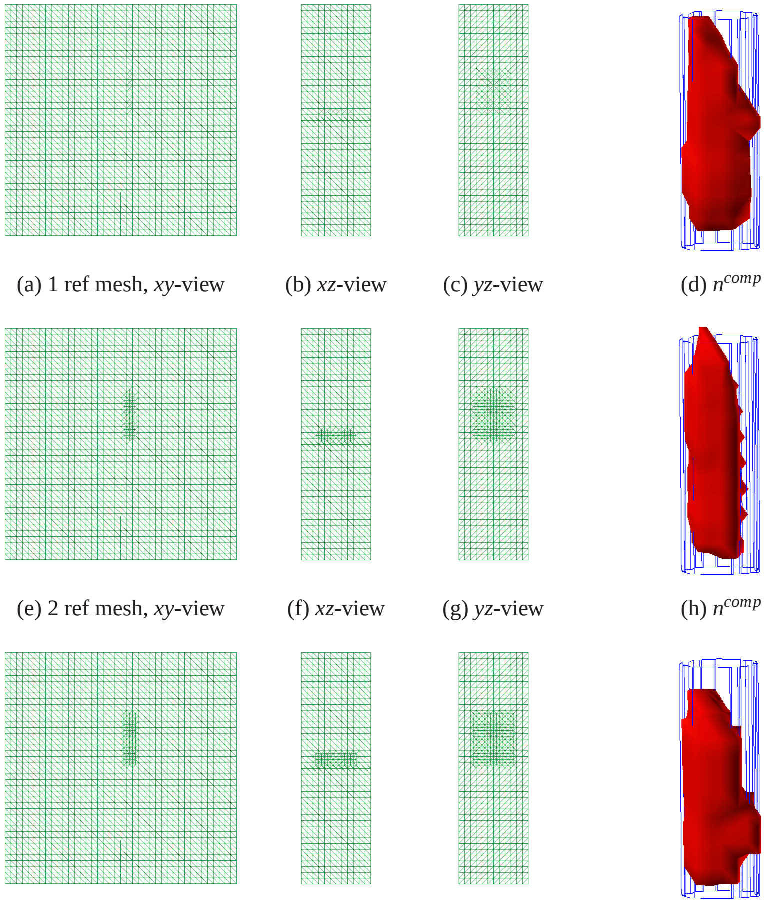

(a) 1 ref mesh, *xy*-view (b) *xz*-view (c) *yz*-view (d) $n^{comp} \approx 4.7$

(e) 2 ref mesh, *xy*-view (f) *xz*-view (g) *yz*-view (h) $n^{comp} \approx 4.7$

(i) 3 ref mesh, *xy*-view (j) *xz*-view (k) *yz*-view (l) $n^{comp} \approx 4.7$

Fig. 5 Adaptively refined meshes for Object #2 of Table 1 and respective reconstructions.

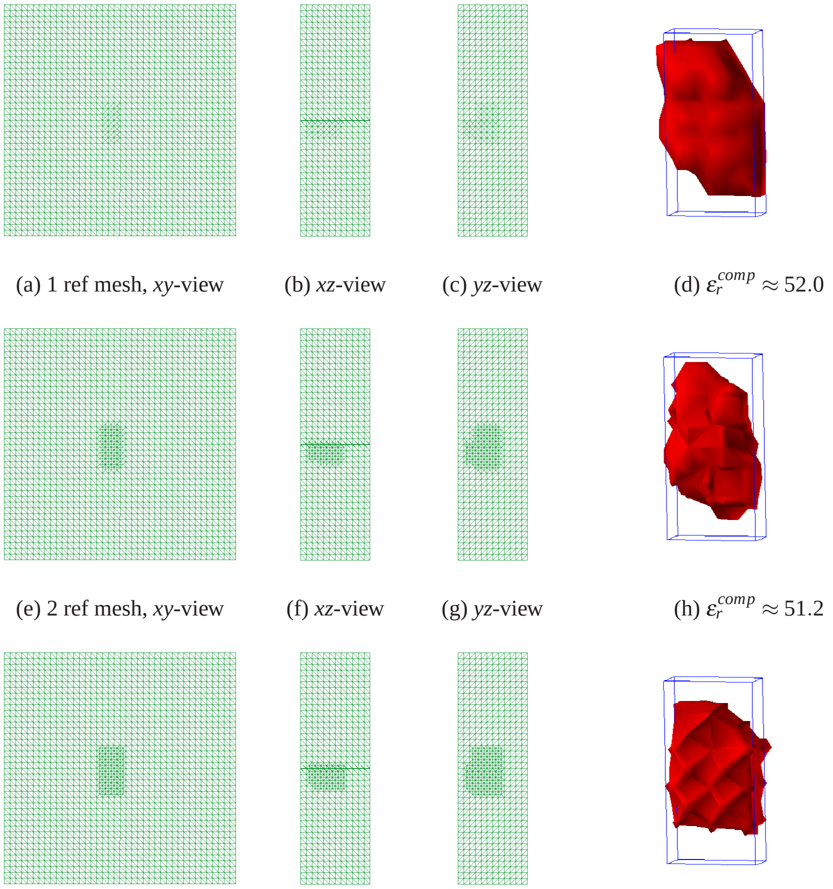

(a) 1 ref mesh, *xy*-view (b) *xz*-view (c) *yz*-view (d) $\varepsilon_r^{comp} \approx 52.0$

(e) 2 ref mesh, *xy*-view (f) *xz*-view (g) *yz*-view (h) $\varepsilon_r^{comp} \approx 51.2$

(i) 3 ref mesh, *xy*-view (j) *xz*-view (k) *yz*-view (l) $\varepsilon_r^{comp} \approx 50.4$

Fig. 6 Adaptively refined meshes for Object #5 of Table 2 and respective reconstructions.

Acknowledgments

This research was supported by US Army Research Laboratory and US Army Research Office grant W911NF-11-1-0399, the Swedish Research Council, the Swedish Foundation for Strategic Research (SSF) through the Gothenburg Mathematical Modelling Centre (GMMC). The computations were performed on resources at Chalmers Centre for Computational Science and Engineering (C3SE) provided by the Swedish National Infrastructure for Computing (SNIC).

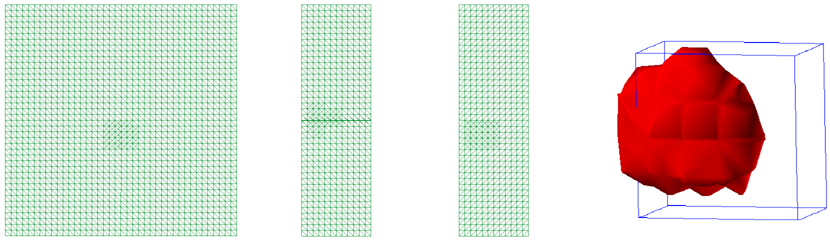

(a) 1 ref mesh, *xy*-view (b) *xz*-view (c) *yz*-view (d) $n^{comp} \approx 4.3$

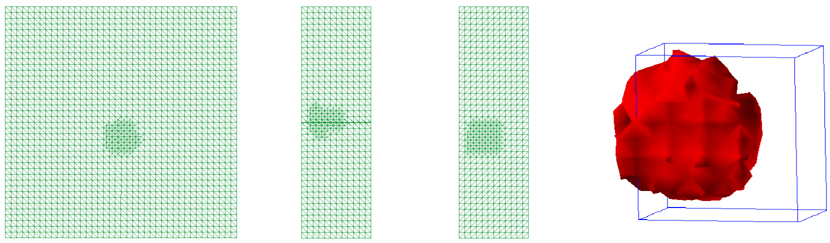

(e) 2 ref mesh, *xy*-view (f) *xz*-view (g) *yz*-view (h) $n^{comp} \approx 4.4$

Fig. 7 Adaptively refined meshes for Object #6 of Table 1 and respective reconstructions.

References

[1] A. Bakushinsky, M. Y. Kokurin, and A. Smirnova. *Iterative Methods for Ill-posed Problems*. Inverse and Ill-Posed Problems Series 54, De Gruyter, 2011.

[2] L. Beilina. Adaptive finite element method for a coefficient inverse problem for the Maxwell's system. *Applicable Analysis*, 90:1461–1479, 2011.

[3] L. Beilina. Energy estimates and numerical verification of the stabilized domain decomposition finite element/finite difference approach for the Maxwell's system in time domain. *Central European Journal of Mathematics*, 11:702–733, 2013.

[4] L. Beilina and C. Johnson. A posteriori error estimation in computational inverse scattering. *Mathematical Models in Applied Sciences*, 1:23–35, 2005.

[5] L. Beilina and M.V. Klibanov. *Approximate Global Convergence and Adaptivity for Coefficient Inverse Problems*. Springer, New York, 2012.

[6] L. Beilina and M.V. Klibanov. Relaxation property for the adaptivity for ill-posed problems. *Applicable Analysis*, 93:223–253, 2013.

[7] L. Beilina, M.V. Klibanov, and M.Yu. Kokurin. Adaptivity with relaxation for ill-posed problems and global convergence for a coefficient inverse problem. *Journal of Mathematical Sciences*, 167:279–325, 2010.

[8] L. Beilina, N. T. Thành, M. V. Klibanov, and M. A. Fiddy. Reconstruction from blind experimental data for an inverse problem for a hyperbolic equation.

Inverse Problems, 30:025002, 2014.

[9] L. Beilina, N. T. Thành, M. V. Klibanov, and J. B. Malmberg. Reconstruction of shapes and refractive indices from backscattering experimental data using the adaptivity. *Inverse Problems*, 30:105007, 2014.

[10] L. Beilina, N. T. Thành, M. V. Klibanov, and J. B. Malmberg. Globally convergent and adaptive finite element methods in imaging of buried objects from experimental backscattering radar measurements. *to appear in Elsevier, Journal of Computational and Applied Mathematics*, 2015.

[11] S. C. Brenner and L. R. Scott. *The Mathematical theory of finite element methods*. Springer-Verlag, Berlin, 2012.

[12] A. L. Bukhgeim and M. V. Klibanov. Uniqueness in the large of a class of multidimensional inverse problems. *Soviet Math. Doklady*, 17:244–247, 1981.

[13] H. W. Engl, M. Hanke, and A. Neubauer. *Regularization of Inverse Problems*. Kluwer Academic Publishers, Boston, 2000.

[14] B. Engquist and A. Majda. Absorbing boundary conditions for the numerical simulation of waves. *Math. Comp.*, 31:629–651, 1977.

[15] M.V. Klibanov, A.B. Bakushinskii, and L. Beilina. Why a minimizer of the Tikhonov functional is closer to the exact solution than the first guess? *J. Inverse and Ill-posed problems*, 19:83–105, 2011.

[16] A. V. Kuzhuget, L. Beilina, M. V. Klibanov, A. Sullivan, L. Nguyen, and M. A. Fiddy. Blind experimental data collected in the field and an approximately globally convergent inverse algorithm. *Inverse Problems*, 28:095007, 2012.

[17] O. Pironneau. *Optimal Shape Design for Elliptic Systems*. Springer-Verlag, Berlin, 1984.

[18] N. T. Thành, L. Beilina, M. V. Klibanov, and M. A. Fiddy. Imaging of buried objects from experimental backscattering radar measurements using a globally convergent inverse algorithm. Preprint, available online at arxiv: 1406.3500, 2014 as well as at Chalmers Publication Library, http://www.math.chalmers.se/Math/Research/Preprints/, preprint number 2014-15.

[19] N. T. Thành, L. Beilina, M. V. Klibanov, and M. A. Fiddy. Reconstruction of the refractive index from experimental backscattering data using a globally convergent inverse method. *SIAM J. Scientific Computing*, 36:B273–B293, 2014.